

● *Original Contribution*

SHEAR WAVE SPEED ESTIMATION USING REVERBERANT SHEAR WAVE FIELDS: IMPLEMENTATION AND FEASIBILITY STUDIES

JUVENAL ORMACHEA,* BENJAMIN CASTANEDA,† and KEVIN J. PARKER*

* Department of Electrical and Computer Engineering, University of Rochester, Rochester, New York, USA; and † Laboratorio de Imagenes Medicas, Pontificia Universidad Catolica del Peru, Lima, Peru

(Received 9 August 2017; revised 9 January 2018; in final form 12 January 2018)

Abstract—Elastography is a modality that estimates tissue stiffness and, thus, provides useful information for clinical diagnosis. Attention has focused on the measurement of shear wave propagation; however, many methods assume shear wave propagation is unidirectional and aligned with the lateral imaging direction. Any deviations from the assumed propagation result in biased estimates of shear wave speed. To address these challenges, directional filters have been applied to isolate shear waves with different propagation directions. Recently, a new method was proposed for tissue stiffness estimation involving creation of a reverberant shear wave field propagating in all directions within the medium. These reverberant conditions lead to simple solutions, facile implementation and rapid viscoelasticity estimation of local tissue. In this work, this new approach based on reverberant shear waves was evaluated and compared with another well-known elastography technique using two calibrated elastic and viscoelastic phantoms. Additionally, the clinical feasibility of this technique was analyzed by assessing shear wave speed in human liver and breast tissues, *in vivo*. The results indicate that it is possible to estimate the viscoelastic properties in each scanned medium. Moreover, a better approach to estimation of shear wave speed was obtained when only the phase information was taken from the reverberant waves, which is equivalent to setting all magnitudes within the bandpass equal to unity: an idealization of a perfectly isotropic reverberant shear wave field. (E-mail: jormache@ur.rochester.edu) © 2018 World Federation for Ultrasound in Medicine & Biology. All rights reserved.

Key Words: Elastography, Shear waves, Reverberant fields, Ultrasound, Tissue stiffness, Shear wave speed estimators.

INTRODUCTION

Elastography is an imaging modality that estimates the bio-mechanical properties of tissues, providing additional useful information for clinical diagnosis (Parker et al. 2011; Shiina et al. 2015). Several elastography modalities have proposed different approaches to measure shear wave speed, shear modulus, and other mechanical parameters (Doyley 2012; Shiina et al. 2015). Particular attention has been focused on the measurement of shear wave propagation; however, reflected waves from organ boundaries and internal inhomogeneities cause modal patterns in continuous wave applications (Parker and Lerner 1992; Taylor et al. 2000) and cause backward traveling waves in transient wave experiments (Ringleb et al. 2005). Reflected waves also

may affect the propagation direction of the induced shear waves; thus, some biased estimates of shear wave speed (SWS) may result because conventional methods for SWS estimation assume shear wave propagation parallel to the lateral direction (Palmeri et al. 2008; Rouze et al. 2010; Song et al. 2014). To address these challenges, directional filters have been applied to avoid some reflections and to isolate shear waves with a different propagation direction (Castaneda et al. 2009; Catheline et al. 2013; Deffieux et al. 2011; Engel and Bashford 2015; Hah et al. 2012; Manduca et al. 2003; McLaughlin and Renzi 2006; Song et al. 2012, 2014; Tzschätzsch et al. 2015; Zhao et al. 2014).

Many continuous shear wave inversion approaches have been developed to estimate the unknown tissue stiffness. These include inversions of the Helmholtz equation in magnetic resonance elastography (MRE) (Oliphant et al. 2001; Ringleb et al. 2005; Van Houten et al. 2001) and sonoelastography (Fu et al. 2000; Parker and Lerner 1992; Yeung et al. 1998). Another class of estimations has been developed for underwater acoustics and geomechanics using

Address correspondence to: Juvenal Ormachea, Department of Electrical and Computer Engineering, University of Rochester, Hopeman Building, Box 270126, Rochester, NY 14627, USA. E-mail: jormache@ur.rochester.edu

random signals (Roux et al. 2005), and these have been extended to noise correlation measurements in soft tissues (Brum et al. 2008, 2015; Catheline et al. 2008, 2013; Gallot et al. 2011). These estimations involve spatial coherence of noise functions measured at two points, and can be recast as Green's functions and time reversal solutions.

Parker et al. (2017) proposed and analyzed a limiting case of a fully reverberant shear wave field in an organ. Mathematically, this limiting case is modeled as the condition where, at an observation point in a tissue, shear waves of random amplitude and phase are found to be propagating in all directions as a statistically isotropic distribution across 4π steradians. Practically speaking, all tissue boundaries with reflections and sources in the vicinity of the observation point contribute to the overall distribution. Analytic solutions were obtained for the expected value of the autocorrelation function for the vector velocity field as a function of space and time, and then for the projection (or dot product) of this along a single direction, taken as the axis of motion detection of an imaging system. From these analytical solutions, the reverberant or diffuse field approach leads to simple estimators of shear wave speed. The mathematical framework and assumptions of a reverberant field are a departure from previous approaches in which directional filters are employed to isolate and characterize one or several principal components of an unknown shear wave field. In contrast, the reverberant or diffuse field explicitly treats a statistically isotropic distribution from all directions, in the imaging plane and out of plane as well, and derives all subsequent processing and estimators from that limiting condition. Thus, strategies for identifying

principal directions and the use of directional filters are obviated.

In this work, the reverberant shear wave field elastography (R-SWE) approach was evaluated and compared with another well-known elastography technique (single-tracking-location shear wave elastography [STL-SWE]) by estimating the SWS in two CIRS-calibrated, elastic and viscoelastic, phantoms. Additionally, the clinical feasibility of the R-SWE modality was analyzed by assessing SWS in human liver and breast tissues, *in vivo*. Moreover, the linear dispersion slope and viscoelastic parameter (extracted from a mechanical model) from each scanned medium were measured for additional characterization of the medium.

METHODS

Experimental setup

To create a reverberant field, multiple sources can be applied to ensure multiple directions of direct and reflected waves. Figure 1(a) illustrates the schematic setup using the breast phantom; a similar setup was used for the custom viscoelastic phantom. Moreover, as illustrated in Figure 1(b), two MISCO loudspeakers were embedded as part of the examination bed used to scan an *in vivo* liver from a volunteer patient. Two power amplifiers (Model 2718, Bruel and Kjaer, Naerum, Denmark; Model BKA1000-4A, ButtKicker, Westerville, OH, USA) and a digital power amplifier (Model LP-2020 A + , Lepai, Bukang, China) driven by a dual-channel function generator (Model AFG3022B, Tektronix, Beaverton, OR, USA)

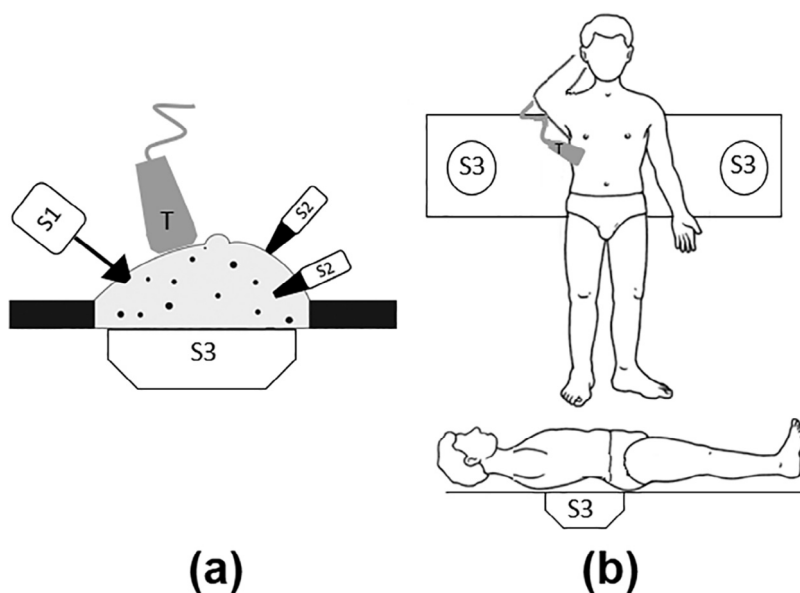


Fig. 1. Schematic setup used in experiments. (a) Three different vibration sources were used for the breast and the viscoelastic phantom. (b) Two MISCO loudspeakers (S3) were coupled to a table for the *in vivo* human liver experiment.

provided input signals to a mechanical vibration source (S1) (Model 4810, Bruel and Kjaer), two miniature vibration sources (S2) (Model NCM02-05-005-4 JB, H2W, Linear Actuator, Santa Clara, CA, USA) and a MISCO loudspeaker (S3) (Model LC62SH-4A, MISCO, Minneapolis, MN, USA), vibrating at different frequencies in contact with a breast phantom (Model 509, CIRS, Norfolk, VA, USA) and a custom shear wave viscoelastic phantom (CIRS). Additionally, an *in vivo* breast tissue experiment was performed with another volunteer patient. In this case, only S1 and two S2 vibration sources were used similar to the setup in Figure 1.

A Verasonics ultrasound system (V-1, Verasonics, Kirkland, WA, USA), which enables high-frame-rate acquisition, and a coherent plane wave compounding acquisition scheme, connected to a linear array ultrasound transducer (Model L7-4, ATL, Bothell, WA, USA), were used to track the induced displacements using a Loupas estimator (Loupas *et al.* 1995). A 3-D matrix of in-phase and quadrature (IQ) data was stored for post-processing. The axial particle velocities are computed from frame-to-frame analysis of the acquired 3-D IQ data. In all experiments, similarly to Parker *et al.* (2017), the center frequency was 5 MHz, 10 cycles of displacements were acquired and the tracking pulse repetition frequency (PRF) was set to acquire at least 18 samples per cycle, that is, $PRF = 18$ times the vibration frequency. Continuous time-harmonic reverberant shear waves were generated into the phantoms and the *in vivo* human liver and breast tissues applying vibrations using single- and multifrequency ranges.

Single-frequency experiments

Vibration frequency (f_v) ranges of 60–450, 60–220 and 40–120 Hz were applied to the breast phantom, viscoelastic phantom and *in vivo* human liver, respectively. For the *in vivo* breast experiment, only a vibration frequency of 180 Hz was used.

Multifrequency experiments

Similarly to Taylor *et al.* (2000) and Tzschätzsch *et al.* (2015), vibrations at different multifrequency ranges were also applied. Thus, 60–100–140, 180–220–260, 300–360–400 and 400–450 Hz was applied to the breast phantom, and 60–80–100 and 140–180–220 Hz to the viscoelastic phantom, respectively. In Figure 2 are snapshots from a movie of a typical reverberant shear wave field in the breast phantom using an f_v of 360 Hz, a multifrequency range of 300–360–400 Hz and the corresponding spectrum signals.

Noise reduction filtering

A 2-D median filter (1.5×1) mm² was applied to each frame for noise spike suppression. Then, a finite impulse

response (FIR) bandpass filter was applied at the temporal frequency domain to remove low-frequency (f_l) and high-frequency (f_h) noise. The cutoff frequencies of the filter were set at $f_l = f_v - 20$ Hz and $f_h = f_v + 20$ Hz, respectively, based on the spectral width of the windowed (temporally limited) time sequence. Subsequently, the magnitude and phase, corresponding to f_v at the frequency domain, was extracted to create a 2-D spatial domain matrix.

In a reverberant field, shear waves propagate in all directions. Thus, applying directional filters to the spatial domain would remove some important information that contributes to the R-SWE generation. However, to remove compressional waves and reduce noise, an additional 2-D FIR bandpass filter to the spatial frequency domain was applied in all directions. The cutoff spatial frequencies, related to the wavenumber (k), of the filter were set at $k_l = 2\pi f_v / c_l$ and $k_h = 2\pi f_v / c_h$, respectively, where c_l and c_h are a chosen low and high SWS, respectively. c_l was 1 m/s for all experiments, whereas c_h was 5 m/s for the breast phantom and *in vivo* breast tissue and 3 m/s for the viscoelastic phantom and *in vivo* human liver. Figure 3 illustrates the spatial frequency spectrum from the 2-D spatial domain matrix, the 2-D spatial bandpass filter and two different profiles at the lateral and axial axes.

Reverberant shear wave field and 2-D shear wave speed estimator

A reverberant shear wave field was created as described under Experimental Setup. The wavenumber and, subsequently, the SWS were estimated using the method described by Parker *et al.* (2017). The wavenumber is obtained based on the equations:

$$|\hat{k}_x|^2 = \frac{5}{\sqrt{2\pi}} \times (\text{Re}\{B_{vv}(0)\} - \text{Re}\{B_{vv}(\Delta x)\}), \quad (1)$$

$$|\hat{k}_z|^2 = 5 \times (\text{Re}\{B_{vv}(0)\} - \text{Re}\{B_{vv}(\Delta z)\}), \quad (2)$$

$$|\hat{k}_{d_1}|^2 = \frac{5}{\sqrt{2\pi}} \times (\text{Re}\{B_{vv}(0)\} - \text{Re}\{B_{vv}(\Delta d_1)\}), \quad (3)$$

$$|\hat{k}_{d_2}|^2 = \frac{5}{\sqrt{2\pi}} \times (\text{Re}\{B_{vv}(0)\} - \text{Re}\{B_{vv}(\Delta d_2)\}), \quad (4)$$

$$k = \sqrt{\frac{\hat{k}_x^2 + \hat{k}_z^2 + \hat{k}_{d_1}^2 + \hat{k}_{d_2}^2}{4}}, \quad (5)$$

where B_{vv} is the 2-D autocorrelation function (13.8×13.8 mm² size) of the reverberant particle velocity signal within the material at $\Delta t = 0$; $B_{vv}(0)$ is evaluated at zero lag. The Δx lag, Δz lag, Δd_1 lag and Δd_2 lag were applied to the lateral, axial, 45° and 135° directions taken from the 2-D correlation window center, respectively.

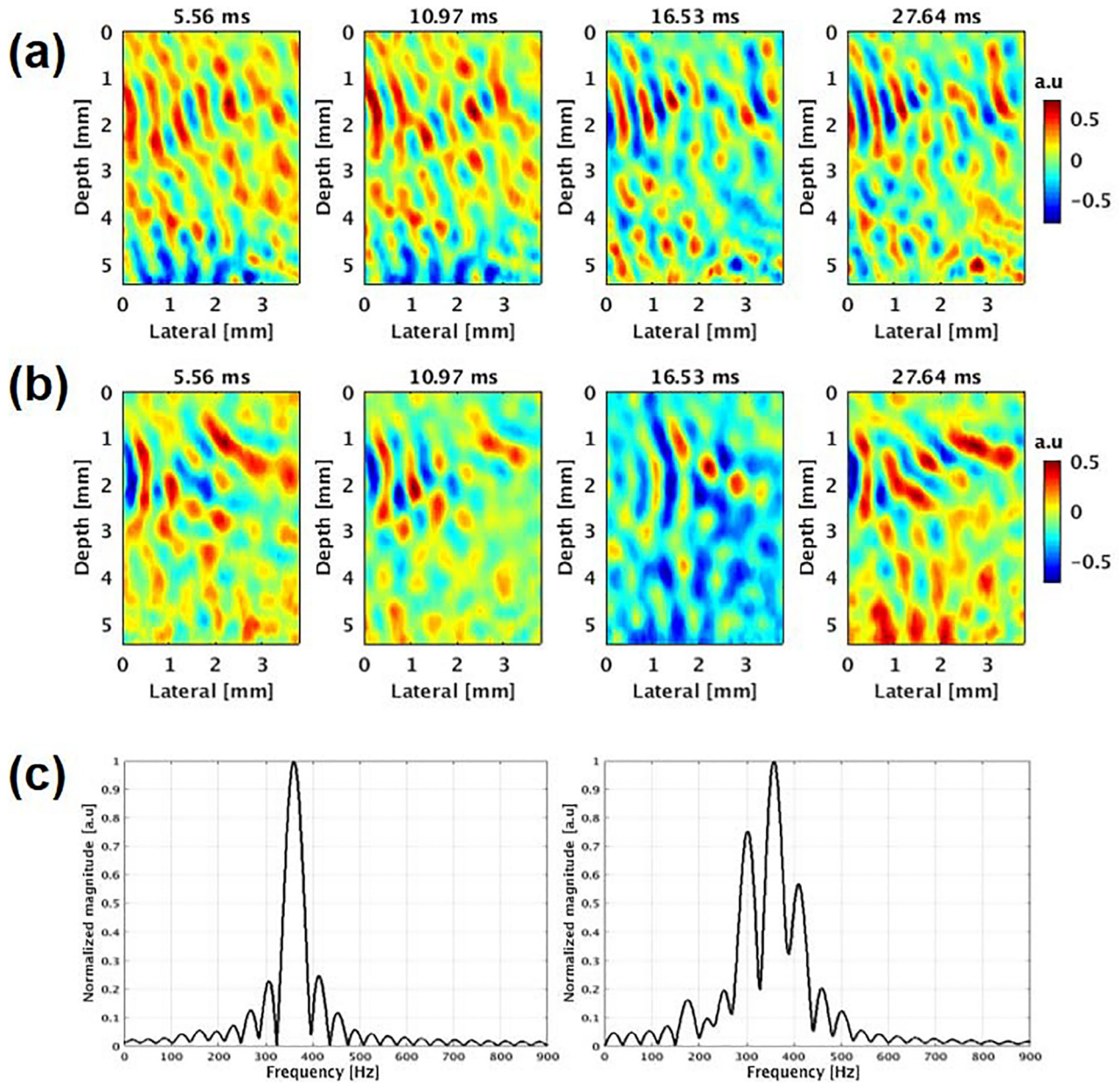


Fig. 2. Snapshots from a movie of a R-SWE generated by multiple vibration sources when (a) only a single $f_v = 360$ Hz was applied and (b) a multifrequency range of 300, 360 and 400 Hz was applied. Number above each frame indicates the time since data acquisition started. (c) Corresponding spectrum signal for cases (a) and case (b), on left and right plots, respectively.

The wavenumber and SWS can then be related using the equation:

$$c_s = \frac{2\pi f_v}{k}, \tag{6}$$

where c_s is the shear wave speed at a given vibration frequency.

Figure 4 illustrates a 2-D autocorrelation result for an arbitrary location within a phantom at $f_v = 360$ Hz and its corresponding autocorrelation profiles for the axial and

lateral directions at the center of the region. Both profiles are in agreement with the theoretical results reported in Parker et al. (2017). Figure 5 summarizes the steps taken to process the R-SWE to obtain the SWS value of a material. In this work two cases were studied. Case 1 applied the R-SWE estimator after the data were processed by the temporal filter. Case 2 applied the R-SWE estimator after application of the temporal filter (of case 1) followed by a spatial filter to further eliminate noise. Furthermore, the spatial filter considered only the phase information, which

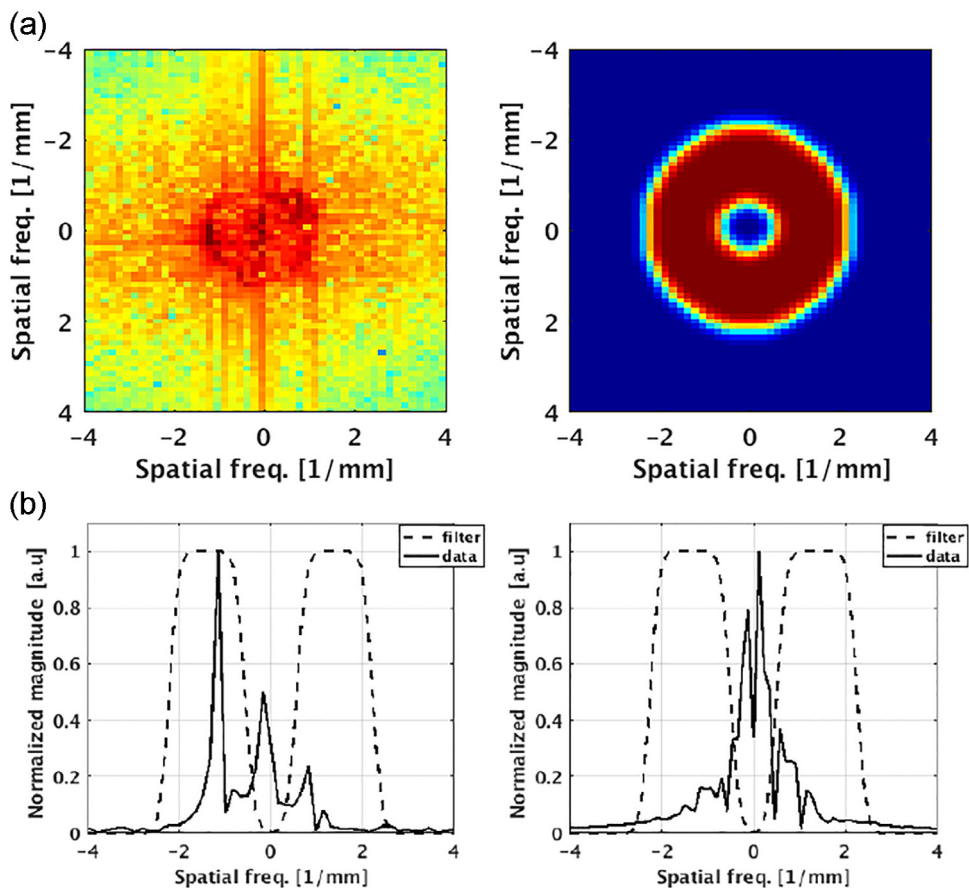


Fig. 3. (a) Left: spatial frequency spectrum. Right: 2-D bandpass filter. (b) Two different profiles from the spatial frequency spectrum and the 2-D filter at the lateral axis (left) and the axial axis (right).

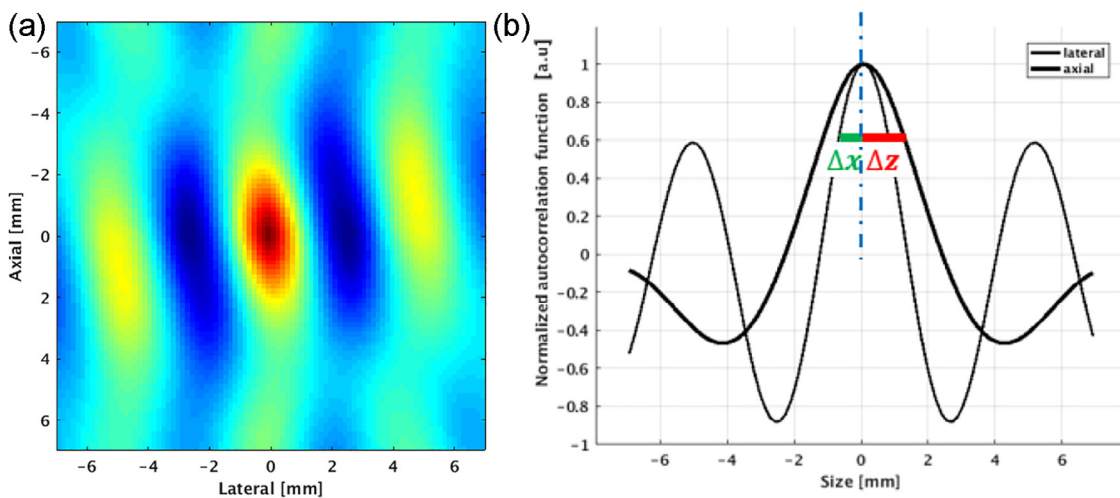


Fig. 4. (a) Two-dimensional autocorrelation map obtained from a chosen location of the R-SWE. (b) Autocorrelation profiles extracted from (a); the *thick line* represents the autocorrelation with respect to z (axial direction), and the *thin line*, the autocorrelation with respect to x (lateral direction). Δx and Δz illustrate the distance from the zero point of the autocorrelation function.

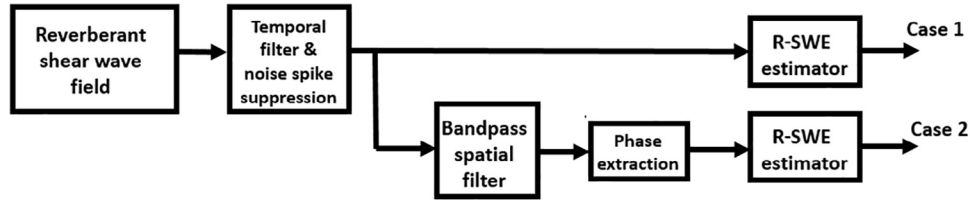


Fig. 5. Flowchart summarizing the steps used to process the reverberant shear wave elastography (R-SWE) data to obtain the shear wave speed for a material.

is equivalent to setting all magnitudes within the bandpass of Figure 3(a) equal to unity: an idealization of a perfectly isotropic reverberant shear wave field.

Phantom study

Homogeneous elastic phantom. The size and shape of the CIRS breast phantom simulate a patient in the supine position; a homogeneous part (20-kPa nominal Young's modulus [E]) from the background region was chosen to evaluate R-SWE. Assuming a perfectly elastic material, c_s can be related to E by:

$$E = 3\rho c_s^2, \quad (7)$$

where ρ is the mass density of the medium (assumed to be 1000 kg/m³) (Parker et al. 2011).

Homogeneous viscoelastic phantom. A CIRS custom-made homogeneous viscoelastic phantom (6-kPa nominal Young's modulus [E]) was chosen to evaluate R-SWE. The rectangular-shaped phantom was protected by a case with openings that allowed contact with the external vibration sources at two lateral borders.

Dispersion estimation. For each phantom, c_s was estimated at different frequencies. Thus, a dispersion (relationship between SWS and frequency) analysis was performed. A linear dispersion slope (dc_s/df) from a chosen frequency range was measured. Additionally, the c_s -versus-frequency curve was fitted to eqn (8) using the MATLAB curve-fitting toolkit (The MathWorks, Natick, MA, USA). In addition, a non-linear least-squares fitting was applied to each curve. The η and α parameter were then obtained:

$$c_s(f) = \sqrt{\frac{E_0 + \eta \cos\left(\frac{\pi\alpha}{2}\right) (2\pi\alpha)^2}{3\rho}}, \quad (8)$$

Here, E_0 refers to the relaxed elastic constant, η refers to the viscoelastic parameter and α refers to the order of the fractional derivative from the Kelvin fractional derivative model (KVFD) (Zhang et al. 2007). As in Zhang et al., the curve-fitting resulted in E_0 close to zero. Thus, it was not included as part of the results of this work.

Inclusion elastic phantom

The CIRS breast phantom contains several solid masses that are at least two times stiffer than the background. A region that contained a 10-mm-diameter inclusion was chosen to evaluate R-SWE at individual f_v between 360 and 450 Hz. A real-time B-mode image was used to guide transducer placement. Then, the contrast and contrast-to-noise ratio (CNR) were evaluated in the SWS images of the inhomogeneous phantoms using the equations:

$$\text{contrast} = \frac{|\bar{c}_{in} - \bar{c}_{out}|}{\bar{c}_{out}}, \quad (9)$$

$$\text{CNR} = \frac{|\bar{c}_{in} - \bar{c}_{out}|}{\sqrt{\sigma_{in}^2 + \sigma_{out}^2}}, \quad (10)$$

where \bar{c}_{in} and \bar{c}_{out} are the mean values of the SWS at rectangular regions within the inclusion and background regions, respectively, and σ_{in} and σ_{out} are the standard deviation for the same regions, respectively.

Shear wave elastography for comparison purposes

Single-tracking-location shear wave elastography (STL-SWE) is a quantitative elastographic technique proposed by McAleavey (Elegbe and McAleavey 2013). In STL-SWE, an acoustic radiation force (ARF) is applied at two locations and involves shear waves tracking in a single location. A Siemens Antares scanner (Siemens Medical Solutions, Malvern, PA, USA) and a Siemens Antares VF7-3 linear array transducer (Siemens Medical Solutions), were used to generate pushing beams as well as to track the induced displacements. The center frequency of both the push and track pulses was 4.21 MHz, the ARF excitation was 200 μ s and the tracking pulse repetition frequency was 7.44 kHz. This technique was used for comparison purposes for the phantom study and it was considered as a reference method in addition to the nominal values reported by the phantom's manufacturer. Although, STL-SWE is a group velocity modality, it is possible to obtain the phase velocity for a specific frequency range using eqn (3) of (Ormachea et al. 2016). Thus, a SWS at 220 Hz was selected in order to compare both elastography approaches.

Clinical application feasibility

Two healthy volunteer patients were scanned to evaluate the feasibility of applying the R-SWE modality to two different *in vivo* experiments (*i.e.*, *in vivo* liver and breast tissue) using the same Verasonics ultrasound system and the linear array ultrasound transducer mentioned before. During the experiment, the patients were laid supine on a custom bed and the right arm abducted, allowing the transducer to access the intercostal and the breast region, respectively. These scans were conducted under the requirements of informed consent and the University of Rochester institutional review board.

RESULTS

Single- and multifrequency comparison

Homogeneous elastic phantom. **Figure 6** shows breast phantom SWS images superimposed on their corresponding B-mode images using the Case 2 processing for a homogeneous region at different f_i . The top row of images show results when only single frequencies were applied; the bottom row of images show results when a multifrequency range was applied. Subsequently, a region of interest (ROI) of $2 \times 1 \text{ cm}^2$ was extracted from the center of each image to obtain the mean SWS and its standard deviation. Additionally, a SWS map (group

velocity image) using STL-SWE is shown for comparison purposes.

Homogeneous viscoelastic phantom. **Figure 7** shows SWS maps superimposed on their corresponding B-mode images using the Case 2 processing for the viscoelastic phantom at different f_i . The top row of images show results when only single frequencies were applied, the bottom row of images show results when a multifrequency range was applied. The same ROI as in the breast phantom experiment was selected here to obtain the SWS mean and its standard deviation. Additionally, a SWS map (group velocity image) using STL-SWE is shown for comparison purposes. It should be noted that the frequency range differs from that used for the breast phantom experiment due to higher shear wave attenuation.

Spatial filter analysis

Homogeneous elastic phantom. **Figure 8(a)** shows the comparison plots of SWS as a function of frequency for Case 1 and Case 2 using the breast phantom and applying single vibration frequencies. The dashed line (nominal SWS) serves as a reference and remains constant for all frequencies. It can be seen that both cases have good agreement with the reference value; however, slightly higher standard deviations were obtained for Case 1. Better

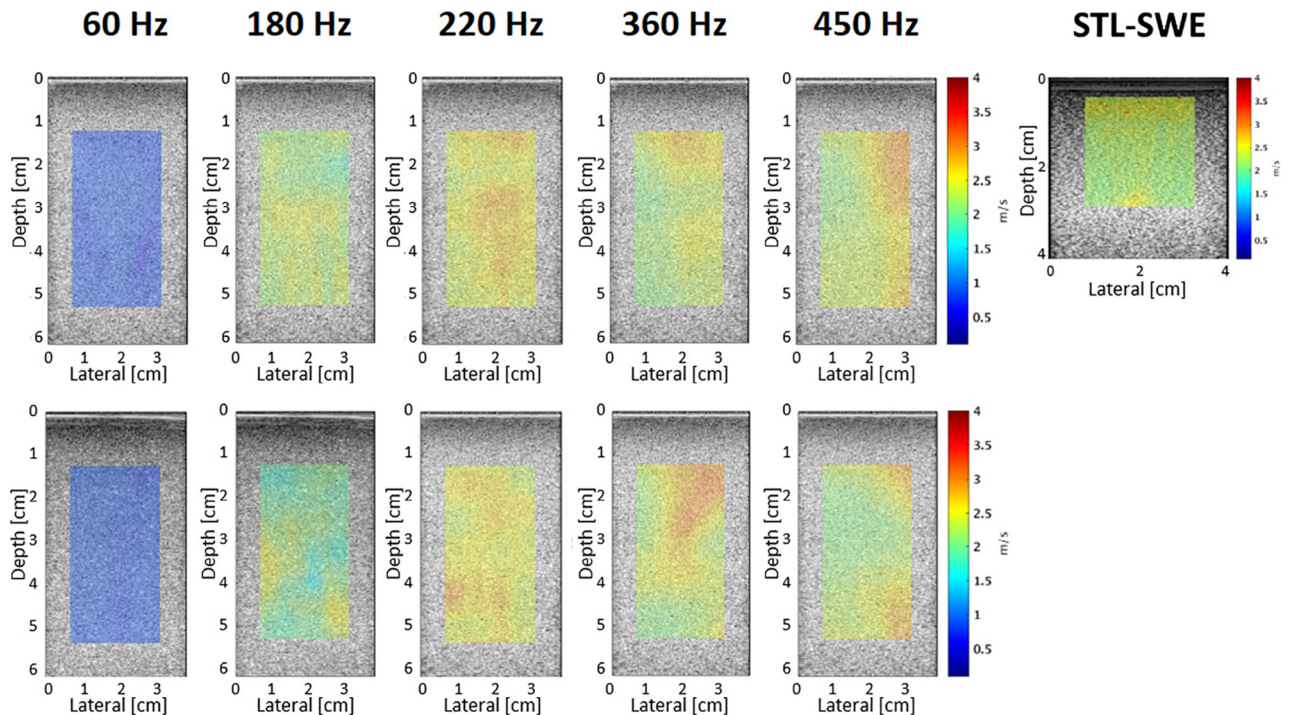


Fig. 6. Shear wave speed (SWS) images superimposed on their corresponding B-mode images for the CIRS breast phantom for case 2. Top row: SWS results when single frequencies were applied. Bottom row: SWS results using a multifrequency range. Number above indicates the corresponding f_i . Top right: Group SWS image using single-tracking-location shear wave elastography (STL-SWE). Frequency range: 180–580 Hz. Peak frequency: 400 Hz.

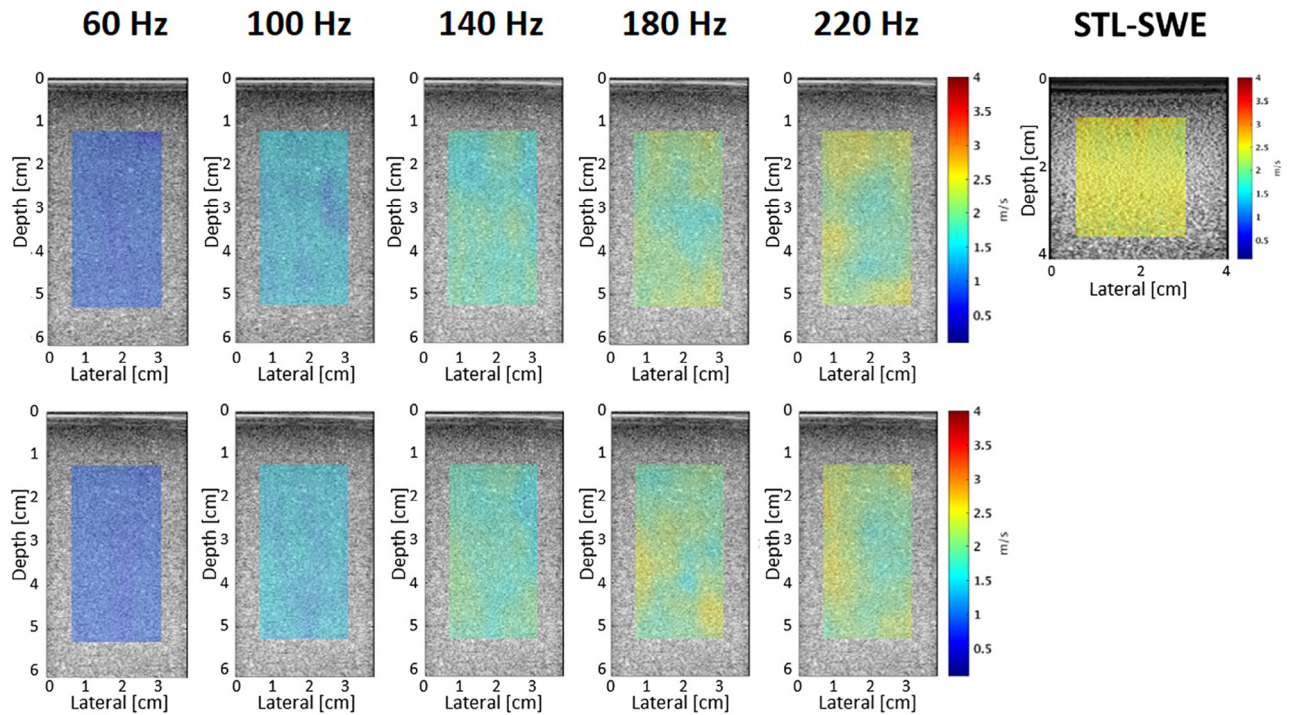


Fig. 7. Shear wave speed (SWS) images superimposed on their corresponding B-mode images for the CIRS custom viscoelastic phantom for case 2. Top row: SWS results when single frequencies were applied. Bottom row: SWS results using a multifrequency range. Number above indicates the corresponding f_v . (Top right) Group SWS image using single-tracking-location shear wave elastography (STL-SWE). Frequency range: 150–350 Hz. Peak frequency: 250 Hz.

agreement compared to the reference was obtained at higher frequencies for both cases. It can be noted that since the breast phantom consists of almost purely elastic material, the SWS results remain nearly constant for the applied vibration frequency range.

Homogeneous viscoelastic phantom. Figure 8(b) shows the comparison plots of SWS as a function of frequency for Case 1 and Case 2 using the viscoelastic phantom and applying single vibration frequencies. The dashed line (nominal SWS) serves as a reference and remains constant for all frequencies. As in the breast phantom, higher standard deviations were obtained for Case 1. It can be noted that since the custom viscoelastic phantom is a dispersive material, the SWS results do not remain constant and they increase with an increasing f_v .

Figure 8 shows the comparison plots of SWS as a function of frequency for Case 2 for the breast phantom (c) and the viscoelastic phantom (d), at single and multi vibration frequencies. The dashed line (nominal SWS) serves as a reference and remains constant for all frequencies. For both cases, good agreement is reported.

Table 1 shows the SWS for the breast phantom. First and second rows indicate the mean and standard deviation for Case 1 and Case 2 applying single f_v . Third and fourth rows show the mean and standard deviation for Case 1 and Case 2 applying multi f_v . Table 2 shows the SWS for the

custom viscoelastic phantom. First and second rows indicate the mean and standard deviation for Case 1 and Case 2 applying single f_v . Third and fourth rows show the mean and standard deviation for Case 1 and Case 2 applying multi f_v . Additionally, the R-SWE modality is compared with STL-SWE at 220 Hz for both phantoms; the difference with respect to the STL-SWE results are presented in Table 3. This comparison is similar to the one reported in (Palmeri et al. 2015). However, in that study, the authors compared the different elastography modalities at 200 Hz.

Dispersion analysis

Table 4 shows the dc_s/df values for each experiment using both CIRS phantoms for a specific frequency range. The minimum f_v was selected in order to have a shorter correspondent wavelength than the 2D window correlation length (*i.e.*, 13.8 mm). For the breast phantom, the dc_s/df results do not differ much between case 1 and case 2 processing using single or multi vibration frequencies. On the other hand, for the viscoelastic phantom, the dc_s/df results show considerable difference between case 1 and case 2 (almost 2 \times) using single and multi vibration frequencies. The dc_s/df values are reasonable since the breast phantom is considered a more elastic material compared with the viscoelastic phantom. Thus, the breast phantom should have lower linear dispersion values compared with

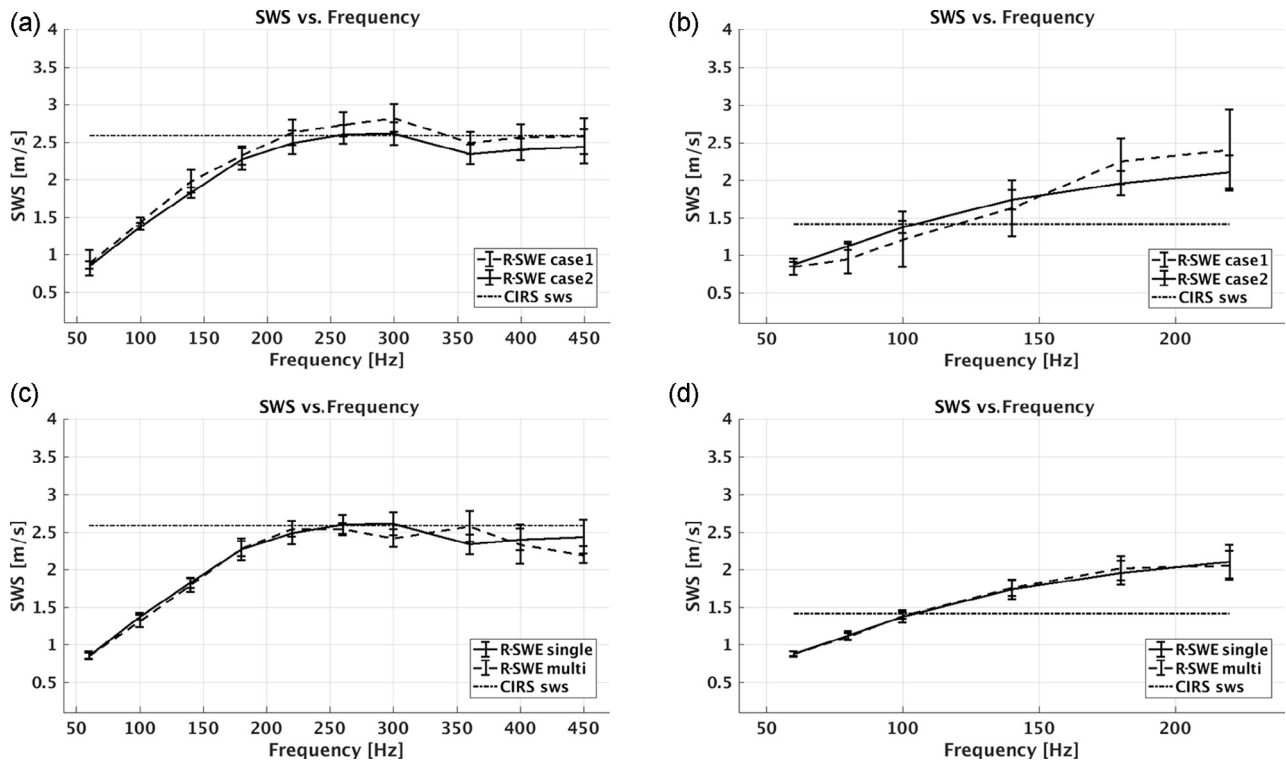


Fig. 8. Comparison plots of shear wave speed (SWS) for cases 1 and 2 for the CIRS breast phantom (a) and CIRS viscoelastic phantom (b), respectively. Comparison plots of SWS for case 2 for the breast phantom (c) and the viscoelastic phantom (d), at single- and multivibration frequencies.

the viscoelastic phantom. Additionally, Table 4 includes the η and α parameters obtained using eqn (8) and the correlation coefficient (R^2) for the KVFD model-fitting. In this case, the η parameter is higher as it corresponds to a more viscoelastic material.

Inclusion elastic phantom

Figure 9 shows breast phantom SWS images at different f_v , resulting from Case 2 processing, all are superimposed on their corresponding B-mode image. Subsequently, one ROI was extracted from the inclusion region ($8 \times 8 \text{ mm}^2$) and two ROI from the background

($8 \times 4 \text{ mm}^2$). The background ROIs were located at each lateral side and at the same depth as the inclusion ROI. The ROIs were selected to obtain contrast and CNR values. Additionally, a SWS map (group velocity image) using STL-SWE is shown for comparison purposes. Table 5 shows the contrast and CNR values for the inclusion phantom using eqns (9) and (10). Better contrast and CNR were obtained as the f_v increased. On the other hand, STL-SWE presents higher contrast, possibly because STL-SWE use a short-time push beam to generate the propagation wave. Thus, its propagating group velocity signal contains a higher frequency range compared with the R-SWE.

Table 1. Measured SWS results for the CIRS breast phantom (homogeneous part)

Type	Value (m/s)	Frequency (Hz)									
		60	100	140	180	220	260	300	360	400	450
Case 1	SWS	0.89	1.44	1.98	2.32	2.63	2.73	2.82	2.49	2.57	2.58
Single	SD	0.17	0.06	0.15	0.12	0.17	0.16	0.19	0.15	0.17	0.24
Case 2	SWS	0.86	1.38	1.83	2.27	2.49	2.60	2.61	2.34	2.40	2.44
Single	SD	0.05	0.05	0.07	0.14	0.16	0.13	0.15	0.13	0.15	0.23
Case 1	SWS	0.88	1.48	1.94	2.44	2.68	2.72	2.63	2.71	2.58	2.39
Multi	SD	0.16	0.25	0.15	0.15	0.11	0.16	0.16	0.17	0.28	0.17
Case 2	SWS	0.85	1.32	1.80	2.28	2.54	2.54	2.42	2.58	2.34	2.20
Multi	SD	0.04	0.09	0.09	0.10	0.10	0.08	0.12	0.20	0.26	0.11

SD = standard deviation, SWS = shear wave speed.

Table 2. Measured SWS results for the CIRS custom viscoelastic phantom

Type	Value (m/s)	Frequency (Hz)					
		60	80	100	140	180	220
Case 1	SWS	0.85	0.95	1.21	1.63	2.25	2.40
Single	SD	0.11	0.20	0.37	0.37	0.30	0.54
Case 2	SWS	0.88	1.12	1.38	1.74	1.96	2.10
Single	SD	0.03	0.06	0.08	0.13	0.16	0.22
Case 1	SWS	0.84	1.11	1.22	1.53	2.14	2.39
Multi	SD	0.08	0.16	0.23	0.35	0.40	0.69
Case 2	SWS	0.88	1.11	1.39	1.76	2.02	2.06
Multi	SD	0.03	0.05	0.05	0.10	0.16	0.19

SD = standard deviation, SWS = shear wave speed.

Table 3. Difference compared with STL-SWE SWS results at 220 Hz

Phantom type	Case	Single	Multi
CIRS	1	17.31%	19.54%
Breast	2	11.06%	13.29%
CIRS	1	9.59%	9.13%
Viscoelastic	2	4.10%	5.94%

STL-SWE = single-tracking location shear wave elastography, SWS = shear wave speed.

Table 5. Contrast and CNR values for the inclusion phantom

	360 Hz	400 Hz	450 Hz	STL-SWE
Contrast	0.12	0.19	0.29	0.91
CNR	1.41	2.78	4.40	8.75

CNR = contrast-to-noise ratio, STL-SWE = single-tracking-location shear wave elastography.

Clinical application

In vivo human liver experiment. For the *in vivo* liver experiment, the same ROI size used in previous experiments was selected (starting at 2.5 cm depth) to obtain the SWS average and standard deviation. The SWS results are in agreement with previous liver studies applying elastography to healthy livers (Ferraioli et al. 2015). The frequency range is lower than that used for the viscoelastic phantom experiment due to higher shear wave attenuation. As reported in the phantom experiments, higher standard deviation was obtained for Case 1 (Table 6). Figure 10 shows SWS images for Case 2, superimposed on their corresponding B-mode images, for the *in vivo* human liver at different f_v . Figure 11 shows the comparison plots of SWS as a function of frequency for Case 1 and Case 2

Table 4. Dispersion results for both CIRS phantoms

Phantom type	Case	Frequency	dc_s/df (m/s/100 Hz)	η (Pa s ^α)	α	R^2	Frequency range (Hz)
CIRS	1	Single	0.39	241.6	0.73	0.92	180–300
Breast		Multi	0.34	545.8	0.57	0.86	
CIRS	2	Single	0.28	546.3	0.54	0.89	180–300
Breast		Multi	0.32	462.7	0.57	0.76	
CIRS	1	Single	1.05	10560	0.99	0.79	100–220
Viscoelastic		Multi	1.03	10180	0.99	0.79	
CIRS	2	Single	0.59	1670	0.99	0.98	100–220
Viscoelastic		Multi	0.56	1080	0.97	0.93	

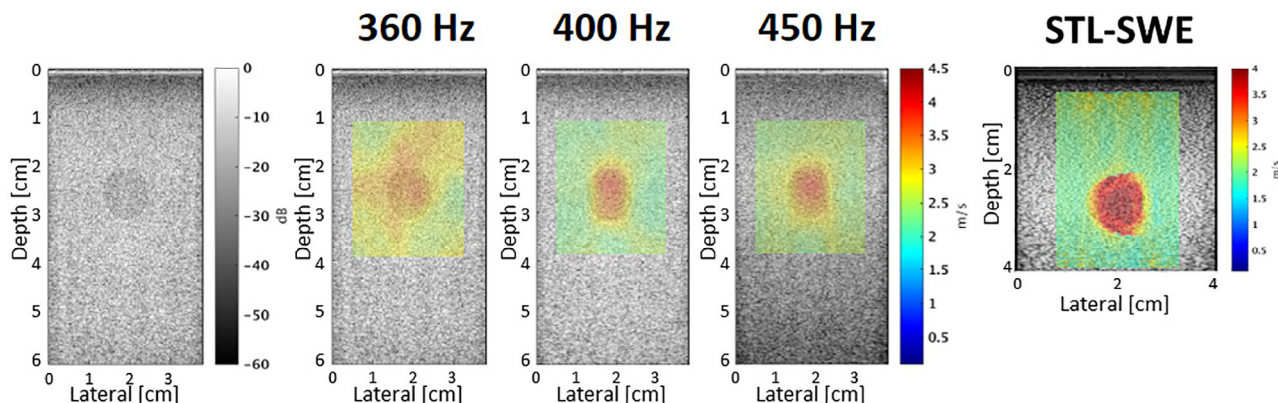


Fig. 9. Shear wave speed (SWS) images superimposed on their corresponding B-mode images for the breast phantom, all of them corresponding to case 2 results. Only a single f_v was applied. Number above indicates the corresponding f_v . Rightmost image: Group SWS image obtained using single-tracking-location shear wave elastography (STL-SWE).

Table 6. Measured SWS results for the *in vivo* human liver experiment

Type	Value (m/s)	Frequency (Hz)						
		40	60	70	80	90	100	120
Case 1	SWS	0.51	0.72	0.94	1.09	1.19	1.20	1.60
Single	SD	0.07	0.13	0.15	0.08	0.15	0.19	0.20
Case 2	SWS	0.60	0.86	1.00	1.10	1.20	1.31	1.46
Single	SD	0.01	0.04	0.04	0.05	0.07	0.06	0.17

SD = standard deviation, SWS = shear wave speed.

and applying single vibration frequencies. The minimum f_v was selected to have a shorter correspondent wavelength than the 2D window correlation length (*i.e.*, 13.8 mm). Table 7 shows the dc/df for Case 1 and case 2. dc/df is higher for Case 2. Additionally, Table 7 includes the η and α parameters obtained using eqn (8). In this case, the η parameter for Case 2 is comparable to that obtained for the viscoelastic phantom when Case 2 was evaluated.

In vivo human breast experiment. For this experiment, two different locations were scanned at $f_v = 180$ Hz. The patient presents fibrocystic breast changes in both breasts. Figure 12 shows the SWS resulting from Case 2 processing. The left image illustrates the presence of the fibrocystic breast changes that have lower SWS than the surrounding area, indicating the presence of a softer tissue. The right image shows a more homogeneous region and reflects a normal breast tissue with a SWS value lower than benign masses reported in (Barr *et al.* 2015).

DISCUSSION

This study evaluated two different processing methods, Case 1 and Case 2. Case 2 includes spatial filtering to

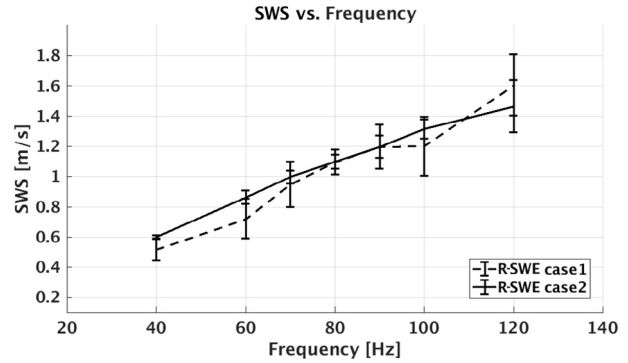


Fig. 11. Comparison plots of shear wave speed (SWS) for cases 1 and 2 for the *in vivo* human liver experiment.

suppress noise and also extracts the phase information in order to set all magnitudes within the band-pass equal to unity: an idealization of a perfectly isotropic R-SWE. For the CIRS breast phantom experiment, the obtained SWS values using Case 1 and Case 2 do not differ much compared to the elasticity nominal value given by the manufacturer. However, they differ with respect to STL-SWE and the linear dispersion slope dc/df . Case 1 presents higher difference with respect to STL-SWE than Case 2 at 220 Hz; for dc/df , Case 1 has higher values than Case 2 using both single and multi vibration frequencies. As expected, the η values indicate a low viscosity value, and the R^2 values for the KVFD model-fitting does not differ much among all results for the elastic material. Although the KVFD fitting parameters show reasonable values for elastic media, all R^2 are less than or equal to 0.92, which indicates that this model does not fit well when an almost purely elastic material is evaluated. Nevertheless, the linear slope dc/df for elastic media indicates a low dispersion,

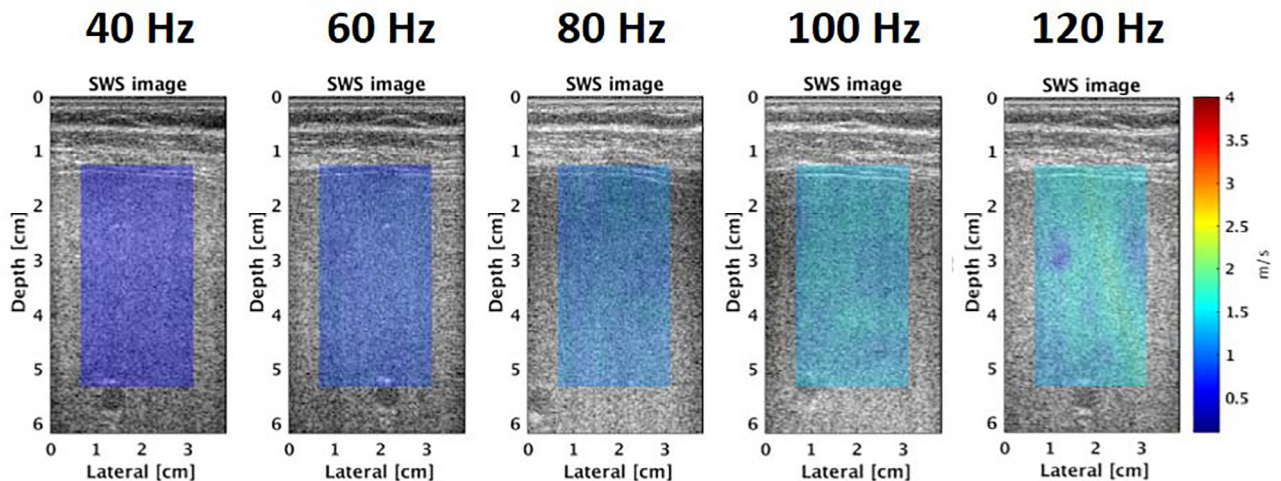


Fig. 10. Shear wave speed (SWS) images superimposed on their corresponding B-mode images for the *in vivo* human liver experiment resulting from case 2 processing. Number above indicates the corresponding f_v .

Table 7. Dispersion results for the *in vivo* human liver experiment

Case	dc_s/df (m/s/100 Hz)	H (Pa s ^α)	α	R^2	Frequency range (Hz)
Case 1	1.46	4567	0.99	0.61	90–120
Case 2	0.87	1285	0.99	0.92	90–120

as expected, for a specific frequency range (*i.e.*, 180 Hz–300 Hz). The differences are more significant between Case 1 and Case 2 for a more viscoelastic material. Similar to the breast phantom results, Case 1 has higher difference with respect to STL-SWE and dc_s/df values than Case 2 using both single and multi f_v . The dc_s/df results in Case 2 are comparable with those reported in (Parker et al. 2015) for a frequency range near 200 Hz. Additionally, the obtained SWS results agree with the SWS results obtained in (Palmeri et al. 2015). In the Palmeri study, a representative phantom that mimics healthy liver tissue at approximately 200 Hz was used. These studies may indicate that the custom CIRS viscoelastic phantom approximates the shear wave dispersion of healthy liver tissue. Additionally, the η results are much higher for Case 1 than Case 2, this may be because Case 1 produced greater SWS estimates with a higher dc_s/df rate (Table 4) than Case 2. The obtained η parameter in Case 1 may indicate that the CIRS phantom is a very viscous material; however, the low estimated R^2 values shows a lower correlation with the KVFD model. Thus, the estimated fitting parameters do not show reliable measurements using Case 1. These results show that Case 2 processing is necessary and appropriate for viscoelastic measurements using the R-SWE. The comparison between both phantoms indicates that the

CIRS breast phantom presents lower dc_s/df and η results which was expected since the viscoelastic phantom is a more dispersive media. Additionally, there are not significant differences between results applying single f_v compared with multi f_v . Thus, the multifrequency approach is feasible and can more quickly assess the frequency dependence of SWS and hence the dispersion and viscoelastic properties than using single f_v , which facilitates the use of this elastography modality for clinical applications. It is worth mentioning that the SWS results are not compared with the nominal values given by the manufacturer because those were obtained using a strain compression test, which only evaluates the low frequency strain/stress material behavior without considering any frequency-dependent material properties. For an elastic media, there is no issue in comparing the SWS with the nominal value due to the relatively low frequency dependence of the material properties.

Figure 8 (a and c) shows a biased estimator when the shear wavelength is larger than the 2D window correlation length (*i.e.*, 13.8 mm). If the nominal value of c_s is considered for the breast phantom, a f_v approximately to 180 Hz is necessary to have shorter shear wavelength than 13.8 mm. Thus, SWS results starting at 180 Hz are closer to the nominal value of c_s as frequency increases. This criteria allow us to choose a minimum f_v to ensure reliable SWS values for all cases, as it can be seen in Tables 4 and 7 for the chosen frequency ranges. To obtain the minimum f_v for the custom viscoelastic phantom and the *in vivo* human liver, the nominal value of c_s and a SWS equal to 1 m/s (a normal SWS for a healthy human liver) were selected, respectively. Figure 8 (b and d) reflects the higher dispersion for the viscoelastic phantom. In this experiment,

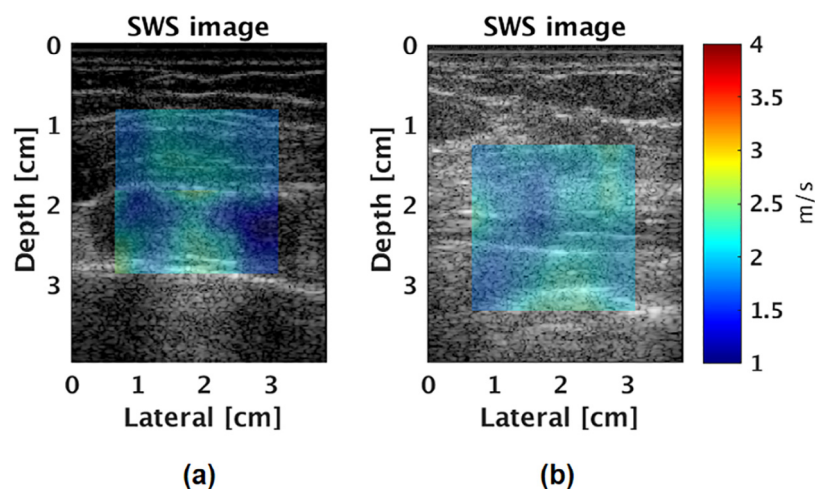


Fig. 12. Shear wave speed (SWS) images superimposed on their corresponding B-mode images for the *in vivo* human breast experiment resulting from case 2 processing. Both images were obtained at $f_v = 180$ Hz on the same breast, but at two different locations. (a) Image revealing the fibrocystic breast changes with SWSs lower than those of the surrounding area. (b) Image revealing a more homogeneous region with a SWS value lower than those of benign masses.

a direct comparison with the CIRS viscoelastic phantom nominal value may not be fair. Thus, it was considered more reasonable to compare the R-SWE results with another modality that has been already characterized. Although STL-SWE is a group velocity modality, it is feasible to obtain the correspondent phase velocity for a specific frequency range. It can also be noted that unlike other modalities, the R-SWE approach does not need to estimate any shear wave propagation direction in order to recover the correct SWS value (the R-SWE indicates that the shear waves propagate for all directions). Therefore, the R-SWE implementation is faster and simpler.

For the inclusion phantom, uneven results were obtained when Case 1 processing was evaluated; thus, only Case 2 is presented and analyzed. R-SWE was able to differentiate both media (softer and harder regions) with similar results as STL-SWE. It was not possible to obtain images of a well-defined inclusion when applying a $f_v = 360$ Hz. This may be because the SWS value for the harder region is approximately 4 m/s (with a correspondent wavelength equal to 1.11 cm), which is longer than the inclusion diameter. Furthermore, as expected, better contrast and CNR results were obtained using higher f_v because the higher the frequency, the shorter the correspondent wavelength. Thus, R-SWE has better capability to differentiate targets. Additionally, the B_{vv} window's size was bigger than the inclusion region; thus, it affects the contrast and CNR estimation for the inclusion phantom. A smaller B_{vv} window's size may contribute to obtain a SWS image with better contrast and CNR values than the reported in this work. However, the same B_{vv} window's size was used for all experiments to keep consistency among all results. On the other hand, since a short ARF pulse is applied, STL-SWE presents a SWS estimation with sharper boundaries for the inclusion due to its better spatial resolution. In addition, the correspondent frequency range for the STL-SWE group velocity was 180–580 Hz with a frequency peak at 400 Hz, higher frequency components than were used with R-SWE.

R-SWE was evaluated in two different *in vivo* human tissues in order to understand its feasibility to estimate viscoelastic properties by generating reverberant shear waves. A future study will apply R-SWE using multi vibration frequencies for *in vivo* experiments. The *in vivo* human liver SWS results ranged between 0.60–1.46 m/s for f_v between 60–120 Hz for Case 2 processing. As expected, these values are in agreement with SWS values reported by (Ferraioli *et al.* 2015). For the *in vivo* human liver experiment, the dc_s/df and the KVFD parameters were measured for Case 1 and 2. For Case 1, dc_s/df was higher than Case 2 for a frequency range of 90 Hz to 120 Hz. The linear slope obtained when Case 2 was applied is comparable with previous dc_s/df results obtained with MRE (*i.e.*, 0.75 m/s/100 Hz at 25 Hz - 63 Hz (Klatt *et al.* 2007)),

however, the frequency ranges are different and cannot be strictly compared. More interesting, using the KVFD fitting parameters to estimate SWS at higher frequencies (Case 2 process), it was found that the SWS is equal to 1.85 m/s with a dc_s/df of 0.46 m/s/100 Hz at 200 Hz. These results are comparable and in agreement with the dispersion results reported in (Parker *et al.* 2015) for the same f_v . These results did not hold true for Case 1. The η result for Case 1 was higher than obtained using Case 2 and the R^2 value was higher for Case 2, which shows a similar behavior as the CIRS viscoelastic phantom. The results obtained using the Case 2 processing are encouraging since the application of R-SWE in *in vivo* liver allows estimation of the SWS and the viscoelastic properties for a region approximately of 3×2 cm². Further study will involve the viscoelastic property estimation for a deeper region using R-SWE modality in fatty patients. R-SWE was also able to measure the SWS in *in vivo* breast tissue using Case 2 processing. Figure 12 shows that R-SWE could assess the fibrocystic breast changes that have lower SWS than the surrounding area and another homogeneous region that reflects normal breast tissue. These values are in agreement with previous studies conducted by (Barr *et al.* 2015). Nevertheless, since malignant lesions in breast tissue have higher SWS values (and it is not as deep as the liver tissue) it is necessary to evaluate R-SWE at higher vibration frequencies than those used in the current experiment. However, R-SWE may have problems in estimating the viscoelastic properties of this tissue due to the high shear wave attenuation as higher frequencies are applied.

As previously mentioned, the reverberant or diffuse field explicitly treats a statistically isotropic distribution from all directions and derives all subsequent processing and estimators from that limiting condition. In that sense, an ideal reverberant field would be obtained using many sources distributed around the region of interest. However, reflections from boundaries and inhomogeneities make this unnecessary in practice. In this study, we had used more vibration sources for the phantoms than *in vivo* experiments due to the easy access to them at any surface. Another reason was the phantom's homogeneous composition, with no internal reflections. These conditions changed for the *in vivo* cases. The access to body surfaces are limited and the tissue inhomogeneity (the presence of layers, bones, fat, different organ sizes, tissue boundaries) cause more reflection waves randomly propagating in different directions, a condition that is needed to create a reverberant field. A more comprehensive determination of shear wave sources remains to be quantified and is left for future research.

Finally, a practical issue for clinicians concerns the time required for data acquisition and processing of the estimator images, particularly for ultrasound systems that are intended for real time operation. High frame rate ultrasound scanning and high complexity shear wave

algorithms are already implemented on a number of ultrasound systems, so the limiting factor may be integration between the vibration sources with the ultrasound system: In this study, there was no integration between the vibration sources and the ultrasound scanner. However, the synchronization and integration between them can be performed by incorporating a master trigger signal. Another limiting factor may be the time required to acquire a satisfactory estimate of the reverberant autocorrelation function. For 100 Hz shear waves, capturing ten cycles of displacements takes 1/10 s, of course fewer cycles could be necessary depending on noise and unwanted tissue motion, however this illustration points to the possibility of reverberant elastography frame rates that are perceived as real time.

CONCLUSIONS

It was possible to estimate the viscoelastic properties in phantom materials and *in vivo* human tissue using the R-SWE approach. The spatial filtering in all directions and the phase signal extraction prove to be important in order to estimate consistent results not only for SWS estimations, but also additional information such the linear dispersion slope or the η parameter from the KVF model, which enables characterization and differentiation of elastic and viscoelastic materials. Moreover, the multifrequency approach shows that it is feasible and can more quickly assess the frequency dependence than using single vibration frequencies, which facilitates the use of the R-SWE approach for clinical applications. Further study will also consider the estimation of the shear wave attenuation coefficient using R-SWE.

Acknowledgments—We thank Professor Stephen A. McAleavey for his help with the STL-SWE experiments. This work was supported by the Hajim School of Engineering and Applied Sciences at the University of Rochester. Juvenal Ormachea was supported by Peruvian Government scholarship 213-2014-FONDECYT.

REFERENCES

Barr RG, Nakashima K, Amy D, Cosgrove D, Farrokh A, Schafer F, Bamber JC, Castera L, Choi BI, Chou YH, Dietrich CF, Ding H, Ferraioli G, Filice C, Friedrich-Rust M, Hall TJ, Nightingale KR, Palmeri ML, Shiina T, Suzuki S, Sporea I, Wilson S, Kudo M. WFUMB guidelines and recommendations for clinical use of ultrasound elastography: Part 2. Breast. *Ultrasound Med Biol* 2015;41:1148–1160.

Brum J, Catheline S, Benech N, Negreira C. Shear elasticity estimation from surface wave: The time reversal approach. *J Acoust Soc Am* 2008;124:3377–3380.

Brum J, Catheline S, Benech N, Negreira C. Quantitative shear elasticity imaging from a complex elastic wavefield in soft solids with application to passive elastography. *IEEE Trans Ultrason Ferroelectr Freq Control* 2015;62:673–685.

Castaneda B, An L, Wu S, Baxter LL, Yao JL, Joseph JV, Hoyt K, Strang J, Rubens DJ, Parker KJ. Prostate cancer detection using crawling wave sonoelastography. *SPIE* 2009;7265:726513.

Catheline S, Benech N, Brum J, Negreira C. Time reversal of elastic waves in soft solids. *Phys Rev Lett* 2008;100:064301.

Catheline S, Souchon R, Rupin M, Brum J, Dinh A, Chapelon JY. Tomography from diffuse waves: Passive shear wave imaging using low frame rate scanners. *Appl Phys Lett* 2013;103:014101.

Deffieux T, Gennisson J, Bercoff J, Tanter M. On the effects of reflected waves in transient shear wave elastography. *IEEE Trans Ultrason Ferroelectr Freq Control* 2011;58:2032–2035.

Doyle M. Model-based elastography: A survey of approaches to the inverse elasticity problem. *Phys Med Biol* 2012;57:R35.

Elegbe EC, McAleavey SA. Single tracking location methods suppress speckle noise in shear wave velocity estimation. *Ultrason Imaging* 2013;35:109–125.

Engel AJ, Bashford GR. A new method for shear wave speed estimation in shear wave elastography. *IEEE Trans Ultrason Ferroelectr Freq Control* 2015;62:2106–2114.

Ferraioli G, Filice C, Castera L, Choi BI, Sporea I, Wilson SR, Cosgrove D, Dietrich CF, Amy D, Bamber JC, Barr R, Chou YH, Ding H, Farrokh A, Friedrich-Rust M, Hall TJ, Nakashima K, Nightingale KR, Palmeri ML, Schafer F, Shiina T, Suzuki S, Kudo M. WFUMB guidelines and recommendations for clinical use of ultrasound elastography: Part 3. Liver. *Ultrasound Med Biol* 2015;41:1161–1179.

Fu D, Levinson S, Gracewski S, Parker K. Non-invasive quantitative reconstruction of tissue elasticity using an iterative forward approach. *Phys Med Biol* 2000;45:1495.

Gallot T, Catheline S, Roux P, Brum J, Benech N, Negreira C. Passive elastography: Shear-wave tomography from physiological-noise correlation in soft tissues. *IEEE Trans Ultrason Ferroelectr Freq Control* 2011;58:1122–1126.

Hah Z, Hazard C, Mills B, Barry C, Rubens D, Parker K. Integration of crawling waves in an ultrasound imaging system: Part 2. Signal processing and applications. *Ultrasound Med Biol* 2012;38:312–323.

Klatt D, Hamhaber U, Asbach P, Braun J, Sack I. Noninvasive assessment of the rheological behavior of human organs using multifrequency mr elastography: A study of brain and liver viscoelasticity. *Phys Med Biol* 2007;52:7281.

Loupas T, Peterson R, Gill RW. Experimental evaluation of velocity and power estimation for ultrasound blood flow imaging, by means of a two-dimensional autocorrelation approach. *IEEE Trans Ultrason Ferroelectr Freq Control* 1995;42:689–699.

Manduca A, Lake DS, Kruse SA, Ehman RL. Spatio-temporal directional filtering for improved inversion of MR elastography images. *Med Image Anal* 2003;7:465–473.

McLaughlin J, Renzi D. Shear wave speed recovery in transient elastography and supersonic imaging using propagating fronts. *Inverse Probl* 2006;22:681.

Oliphant TE, Manduca A, Ehman RL, Greenleaf JF. Complex-valued stiffness reconstruction for magnetic resonance elastography by algebraic inversion of the differential equation. *Magn Reson Med* 2001;45:299–310.

Ormachea J, Lavarello RJ, McAleavey SA, Parker KJ, Castaneda B. Shear wave speed measurements using crawling wave sonoelastography and single tracking location shear wave elasticity imaging for tissue characterization. *IEEE Trans Ultrason Ferroelectr Freq Control* 2016;63:1351–1360.

Palmeri M, Nightingale K, Fielding S, Rouze N, Deng Y, Lynch T, Chen S, Song P, Urban M, Xie H, Wear K, Garra B, Milkowski A, Rosenzweig S, Carson P, Barr R, Shamsdasani V, Macdonald M, Wang M, Guenette G, Miyajima Y, Okamura Y, Dhyani M, Samir A, Hah Z, McLaughlin G, Gee A, Chen Y, Napolitano D, McAleavey S, Obuchowski N, Hall T. RSNQ QIBA ultrasound shear wave speed phase II phantom study in viscoelastic media. *Proc IEEE Int Ultrason Symp* 2015;1–4.

Palmeri ML, Wang MH, Dahl JJ, Frinkley KD, Nightingale KR. Quantifying hepatic shear modulus in vivo using acoustic radiation force. *Ultrasound Med Biol* 2008;34:546–558.

Parker KJ, Lerner RM. Sonoelasticity of organs: Shear waves ring a bell. *J Ultrasound Med* 1992;11:387–392.

Parker KJ, Doyle MM, Rubens DJ. Imaging the elastic properties of tissue: The 20 year perspective. *Phys Med Biol* 2011;56:R1.

- Parker KJ, Partin A, Rubens DJ. What do we know about shear wave dispersion in normal and steatotic livers? *Ultrasound Med Biol* 2015; 41:1481–1487.
- Parker KJ, Ormachea J, Zvietcovich F, Castaneda B. Reverberant shear wave fields and estimation of tissue properties. *Phys Med Biol* 2017; 62:1046.
- Ringleb SI, Chen Q, Lake DS, Manduca A, Ehman RL, An KN. Quantitative shear wave magnetic resonance elastography: Comparison to a dynamic shear material test. *Magn Reson Med* 2005;53:1197–1201.
- Roux P, Sabra KG, Kuperman WA, Roux A. Ambient noise cross correlation in free space: Theoretical approach. *J Acoust Soc Am* 2005; 117:79–84.
- Rouze NC, Wang MH, Palmeri ML, Nightingale KR. Robust estimation of time-of-flight shear wave speed using a radon sum transformation. *IEEE Trans Ultrason Ferroelectr Freq Control* 2010; 57:2662–2670.
- Shiina T, Nightingale KR, Palmeri ML, Hall TJ, Bamber JC, Barr RG, Castera L, Choi BI, Chou YH, Cosgrove D, Dietrich CF, Ding H, Amy D, Farrokh A, Ferraioli G, Filice C, Friedrich-Rust M, Nakashima K, Schafer F, Sporea I, Suzuki S, Wilson S, Kudo M. WFUMB guidelines and recommendations for clinical use of ultrasound elastography: Part 1. Basic principles and terminology. *Ultrasound Med Biol* 2015;41:1126–1147.
- Song P, Zhao H, Manduca A, Urban MW, Greenleaf JF, Chen S. Comb-push ultrasound shear elastography (CUSE): A novel method for two-dimensional shear elasticity imaging of soft tissues. *IEEE Trans Med Imaging* 2012;31:1821–1832.
- Song P, Manduca A, Zhao H, Urban MW, Greenleaf JF, Chen S. Fast shear compounding using robust 2-D shear wave speed calculation and multi-directional filtering. *Ultrasound Med Biol* 2014;40:1343–1355.
- Taylor L, Porter B, Rubens D, Parker K. Three-dimensional sonoelastography: Principles and practices. *Phys Med Biol* 2000; 45:1477.
- Tzschätzsch H, Ipek-Ugay S, Trong MN, Guo J, Eggers J, Gentz E, Fischer T, Schultz M, Braun J, Sack I. Multifrequency time-harmonic elastography for the measurement of liver viscoelasticity in large tissue windows. *Ultrasound Med Biol* 2015;41:724–733.
- Van Houten EE, Miga MI, Weaver JB, Kennedy FE, Paulsen KD. Three-dimensional subzone-based reconstruction algorithm for mr elastography. *Magn Reson Med* 2001;45:827–837.
- Yeung F, Levinson SF, Fu D, Parker KJ. Feature-adaptive motion tracking of ultrasound image sequences using a deformable mesh. *IEEE Trans Med Imaging* 1998;17:945–956.
- Zhang M, Castaneda B, Wu Z, Nigwekar P, Joseph JV, Rubens DJ, Parker KJ. Congruence of imaging estimators and mechanical measurements of viscoelastic properties of soft tissues. *Ultrasound Med Biol* 2007;33:1617–1631.
- Zhao H, Song P, Meixner DD, Kinnick RR, Callstrom MR, Sanchez W, Urban MW, Manduca A, Greenleaf JF, Chen S. External vibration multi-directional ultrasound shearwave elastography (EVMUSE): Application in liver fibrosis staging. *IEEE Trans Med Imaging* 2014; 33:2140–2148.